Article

Investigation of Flow-Induced Noise Characteristics in the Oblique Flow Pump

Zhengxuan Xu [1], Feifei Zhao [1], Jia Liu [1], Fan Zhang [1,*], Jinfeng Zhang [1] and Mengbin Song [2]

1   National Research Center of Pumps, Jiangsu University, Zhenjiang 212013, China
2   LEO Group Co., Ltd., Taizhou 317500, China
*   Correspondence: fzhang@ujs.edu.cn; Tel.: +86-18752962351

Abstract: An oblique flow pump is widely used in farmland irrigation and drainage, water transfer projects, thermal power generation, and other fields. However, unstable flow factors in the oblique flow pump easily lead to pump vibration and noise. To improve the stability of pump operation and optimize the operating environment, it is necessary to study the flow-induced noise characteristics of oblique flow pumps. In this paper, CFD and noise simulation software are used to calculate the flow field and sound field of the oblique flow pump. The internal flow characteristics and flow-induced noise characteristics of the oblique flow pump were studied. The results show that when the flow rate of the oblique flow pump deviates from the optimal operating point, especially in the small flow rate, due to the phenomena of backflow and flow separation, more high-energy vortices are produced in the flow channel, and the vortices are distributed in a wide area, which will cause greater flow-induced noise. It is found that with the increase in flow rate, the sound pressure level of flow noise in the inlet channel gradually decreases, the sound pressure level in the guide vane region first decreases and then increases, and the sound pressure level is the lowest at 1.0Q. Generally speaking, the noise sound pressure level in the outlet channel region of the pump also gradually decreases. In addition, at the blade frequency, the radiated noise of the oblique flow pump can show dipole characteristics under various flow conditions, and the radiation level of sound pressure increases with the increase in flow rate. This paper can provide a theoretical basis for the mechanism research and control strategy of flow-induced noise in oblique flow pumps.

Keywords: oblique flow pump; vortex; flow-induced noise; flow separation

1. Introduction

The oblique flow pump is widely used in farmland irrigation and drainage, water transfer engineering, thermal power generation, and other fields because of its advantages of good cavitation resistance, wide efficiency area, compact structure, and convenient start-up [1,2]. The coherent action between the inlet flow of the impeller and the rotating flow field of the impeller, the dynamic and static interference between the outlet fluid of the impeller and the guide vane, the rotating stall and cavitation of the guide vane, and other unstable flow factors are easy to cause pump vibration and noise, which will not only affect the operation stability of the unit [3,4] but also destroy the environment and affect people's health. To improve the stability of pump operation and optimize the operating environment, it is necessary to study the flow-induced noise characteristics of oblique flow pumps.

At present, many domestic and foreign scholars have carried out research on flow-induced noise. Some scholars have studied the flow-induced noise characteristics of centrifugal pumps under different operating conditions. Dong et al. [5] took a centrifugal pump as a turbine as the research object; based on the acoustic–vibration coupling method, the external field flow-induced noise produced by fluid-excited structural vibration is calculated, and the contribution of external field sound source in each frequency band

is evaluated. The results show that the flow-induced noise caused by the shell dipole contributes the most to the external field noise, followed by the flow noise caused by the shell dipole, and the flow-induced noise caused by the impeller dipole contributes the least to the external field noise. Guo et al. [6] carried out numerical calculation and an experiment on the internal field noise of jet centrifugal pump, studied the characteristics of flow noise and flow-induced noise of the model pump, and analyzed that the noise induced by an impeller rotating dipole sound source reached the maximum at shaft frequency, which played a leading role in the internal field noise of a jet centrifugal pump. He et al. [7] studied the internal flow characteristics and noise characteristics of a centrifugal pump under gas–liquid two-phase flow, and they compared and analyzed the influence of different inlet gas volume fractions on the internal flow-induced noise of the pump. Si et al. [8] studied the flow-induced noise characteristics of a high-speed centrifugal pump. The results show that the frequency spectrum of fluid noise at the pump outlet shows wide frequency band characteristics, but there are obvious discrete peaks, which are related not only to the fluid pressure pulsation characteristics in the low-frequency region but also to the structural modal frequency. The rotor–stator flow field interaction between the impeller and volute is the main cause of flow-induced noise. Some scholars have studied the factors affecting the flow-induced noise of centrifugal pumps and put forward the scheme of optimizing the noise, Wang et al. [9] studied the influence of the number of blades on the flow-induced noise of a centrifugal pump. The results show that the diaphragm is the main noise source of the centrifugal pump. With the increase in the number of blades, the sound pressure level of the model pump first decreases and then increases, and it reaches the minimum when the number of blades is 6. Choi et al. [10] separately analyzed the unsteady flow characteristics of a centrifugal pump impeller with air as working medium without volute and guide vane, and they expounded the relationship between unsteady flow field and radiated noise characteristics of the impeller. Dai et al. [11] made a bionic modification on centrifugal pump blades, and they compared and analyzed the effects of different bionic structures on the noise reduction performance of centrifugal pumps. The results show that the pit structure has little influence on external characteristic parameters, while the sawtooth structure has a relatively great influence. The noise reduction effect of the pit structure is aimed at broadband noise, while the sawtooth structure is aimed at discrete noise of blade passing frequency and its frequency doubling.

The above-mentioned research mainly focuses on the flow-induced noise in centrifugal pumps and its influencing factors. Some scholars have also studied the flow-induced noise in axial flow pumps [12], axial piston pumps [13] and water jet propulsion pumps [14], and some scholars have studied the flow noise in an axial flow pump station [15], but there are few related studies on oblique flow pumps, and few articles have studied the flow-induced noise characteristics in oblique flow pumps. As a kind of common hydraulic machinery, domestic and foreign scholars have mainly focused on the unsteady flow characteristics in the pump [16–18], the pressure pulsation characteristics in the whole flow channel [19], the factors affecting the pump performance [20] and the vibration characteristics of the pump impeller [21], but few scholars have analyzed the relationship between the internal flow characteristics of the oblique flow pump and the flow-induced noise. Therefore, this paper takes the oblique flow pump as the research object, carries out the unsteady flow numerical calculation, analyzes the flow field in the pump, and further studies the flow-induced noise characteristics in the pump.

2. Materials and Methods

2.1. Geometric Model

In this paper, an oblique flow pump is taken as the research object, and its main design parameters are as follows. The flow rate Q is 1273.3 m^3/h, the head H is 14.08 m, the speed n is 1450 r/min, the impeller is semi-open, the inlet diameter $D1$ is 350 mm, the outlet diameter $D2$ is 400 mm, the number of impeller blades $Z1$ is 4, and the number of guides vane blades $Z2$ is 7. UG software is used to extract water from the whole flow channel

of the oblique flow pump assembly, and the fluid domain is divided into an inlet section, impeller, guide vane, and outlet section. As shown in Figure 1 [22], the calculation area is the whole device section from the inlet section to the outlet section of the pump. The model pump conveys clear water with a density of 1 g/cm^3 at room temperature. The pump body material is ZG230-450 with a density of 7830 kg/m^3, elastic modulus of 211 GPa, and Poisson's ratio of 0.311.
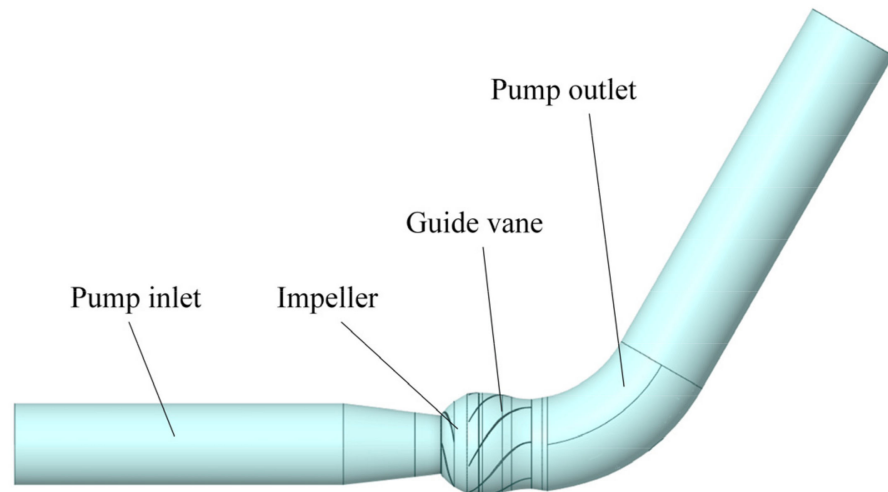
Figure 1. Computational domain of whole flow passage.

2.2. Grid Division of the Fluid Computational Domain

In this paper, ANSYS Mesh software is used to divide the computational domain into grids, and the grid type is selected as a hybrid grid. To better simulate the flow near the wall, a boundary layer grid is used in the near-wall region, and the average y^+ value in the near-wall region is controlled within 100 by local encryption of key parts such as blades. The specific division is shown in Figure 2 [22]. The grid independence of an oblique flow pump under optimal working condition and steady flow is verified as shown in Figure 3 [22], and the total number of grids in the fluid domain is finally determined to be 11.09 million.
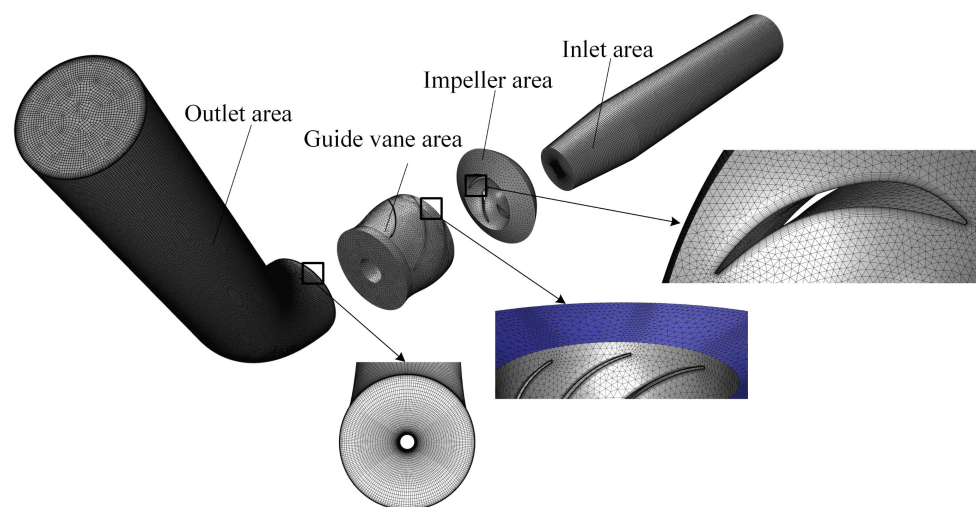
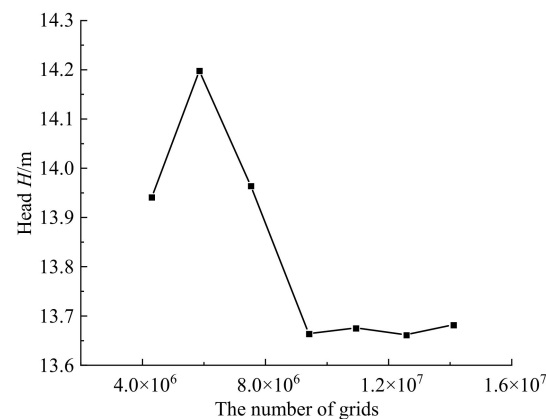**Figure 2.** Mesh generation of the computational domain.

Figure 3. Influence of mesh number on the pump head.

2.3. CFD Computational Turbulence Model and Boundary Conditions

The whole fluid domain is simulated by ANSYS CFX software. The turbulence model SST k-ω model combines the advantages of the standard k-ω model in the near-wall region and the standard k-ε model in the free shear layer. Therefore, the SST k-ω model is used for simulation calculation in this paper. The k-equation and ω-equation of SST k-ω model are [23]:

$$\frac{\partial(\rho k)}{\partial t} + \frac{\partial(\rho k u_i)}{\partial x_i} = \frac{\partial}{\partial x_j}\left[\left(\mu + \frac{\mu_t}{\sigma_{k3}}\right)\frac{\partial k}{\partial x_j}\right] + p_k - \beta^* \rho k \omega \tag{1}$$

$$\frac{\partial(\rho \omega)}{\partial t} + \frac{\partial(\beta \omega u_i)}{\partial x_i} = \frac{\partial}{\partial x_j}\left[\left(\mu + \frac{\mu_t}{\sigma_{\omega3}}\right)\frac{\partial \omega}{\partial x_j}\right] + \alpha_3 \frac{\omega}{k}p_k - \beta_3 \rho \omega^3 + 2(1 - F_1)\rho \frac{1}{\omega \sigma_{\omega2}}\frac{\partial k}{\partial x_j}\frac{\partial \omega}{\partial x_j} \tag{2}$$

In the formula:

$$\mu_t = \rho \frac{a_1 k}{max(a_{1\omega}, SF_2)} \tag{3}$$

$$P_k = \mu_t \left(\frac{\partial u_i}{\partial x_j} + \frac{\partial u_j}{\partial x_i}\right)\frac{\partial u_i}{\partial x_j} - \frac{2}{3}\frac{\partial u_k}{\partial x_k}\left(3\mu_t \frac{\partial u_k}{\partial x_k} + \rho k\right) \tag{4}$$

where P_k is the turbulence generation term caused by viscous force.

Equations (1) and (2) combine the corresponding equations of the Wilcox k-ω model and standard k-ε model by mixing functions. The constant, Φ_3, is calculated as follows:

$$\Phi_3 = F_1\Phi_1 + (1 - F_1)\Phi_2 \tag{5}$$

where Φ_1 is the Wilcox k-ω model constant; Φ_2 is the standard k-ε model constant; F_1 is a mixed function, when near the wall, F_1 = 1, and F_1 = 0 when far away from the wall. The F_1 expression is:

$$F_1 = \tan h\left(\xi^4\right) \tag{6}$$

$$\xi = min\left[max\left(\frac{\sqrt{k}}{\beta^* \omega d_w}, \frac{500\mu}{\rho d_w^2 \omega}\right), \frac{4\rho k}{D_w^+ \sigma_{\alpha2}^2 d_w^2}\right] \tag{7}$$

$$D_\omega^+ = max\left[2\rho \frac{1}{\sigma_{\omega2}}\frac{1}{\omega}\frac{\partial k}{\partial x_j}\frac{\partial j}{\partial x_j}, 10^{-10}\right] \tag{8}$$

F_2 is also a mixed function, and its function is similar to F_1, which is 1 in the boundary layer and 0 in the shear layer;

$$F_2 = \tan h\left(\eta^2\right) \tag{9}$$

$$\eta = max\left\{\frac{2k^{1/2}}{\beta^*\omega d_w}, \frac{500\mu}{\rho d_w^2 \omega}\right\} \tag{10}$$

Among the above formulas: β^* is the empirical coefficient, which is often 0.09; d_w is the distance from the calculation point to the wall, which is equivalent to d in the Spalart–Allmaras model; a1 is the empirical coefficient, taking 0.31; and S is the value of the strain rate tensor; other related constants are: $\alpha_1 = 5/9$, $\beta_1 = 0.075$, $\sigma_{k1} = 1.176$, $\sigma_{\omega1} = 2$, $\alpha_2 = 0.44$, $\beta_2 = 0.0828$, $\sigma_{k2} = 1$, $\sigma_{\omega2} = 1/0.856$.

The impeller of the oblique flow pump was set as the rotating domain, and the remaining parts were set as the static domain. In steady calculation, the front and rear parts of the impeller are, respectively, connected with the inlet pipe and the guide vane, and the interface type is set as a frozen rotor. In unsteady calculation, the static and dynamic interface is set as a transient rotor stator. The inlet boundary condition is set as the pressure inlet, and the outlet is set as the mass flow outlet. The wall of the static area is set to the smooth wall condition without slip. To improve the stability and convergence speed of the calculation, the steady calculation is carried out first, and then, the steady result is taken as the initial value of the unsteady calculation. The unsteady calculation time step is 3 degrees of the impeller rotation, that is, 0.000344828 s per step, and the total calculation time is 15 times the impeller rotation period, with a total of 1800 steps (0.62069 s). The calculation results of the last five cycles are selected to analyze the internal flow field and flow-induced noise characteristics.

2.4. Validation between Computational Fluid Dynamics and Experiment

2.4.1. Experiment Device and Method

The performance test of the oblique flow pump was carried out on the multifunctional pump model and device model test bench at the National Pumps Research Center of Jiangsu University. The installation of the test device system is shown in Figure 4 [22]. The flow rate of the test device is measured by an intelligent electromagnetic flowmeter, and the measurement accuracy is better than ±0.2%; The head is measured by installing a differential pressure transmitter on the device. The type of differential pressure transmitter is a WT2000DP5S intelligent differential pressure transmitter, and the measurement uncertainty is better than ±0.1%. The torque and speed are measured by ZJYW1/ZJ500Nm intelligent torque and speed sensor, and the accuracy is better than ±0.1%. When the sensor is used, it only bears torque and does not bear other external forces.

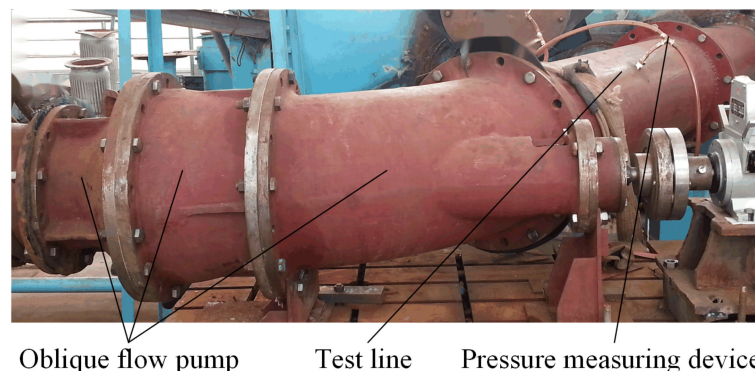Oblique flow pump   Test line   Pressure measuring device

Figure 4. Test device system.

Before the efficiency test, run the pump at the rated working point for more than 30 min to eliminate the free gas in the circulation system, and check the bearing, seal, noise, and vibration of the pump. Performance tests shall be conducted without cavitation. At the beginning of the test, the valve needs to be adjusted to a fully open state, and then, the measurement is carried out. The test points shall be reasonably distributed on the whole performance curve, and the number of test points in the test curve shall not be less than 15. After the test condition is stable, the test system is continuously tested three times without

any artificial interference, and the test time is 30 s each time. The difference between the maximum and minimum efficiency of the three tests should be less than 0.3%. Otherwise, the test needs to be carried out again, and the intermediate value of the three measurements should be taken as the final test result.

2.4.2. Comparative Analysis of Numerical Calculation and Experiment

The comparison curve between the experimental external characteristic results and the numerical simulation results is shown in Figure 5 [22]. It can be seen from the curve in the figure that the trend of numerical calculation results is basically consistent with the experimental measurement results, and the shaft power simulated by numerical calculation is consistent with the experimental measurement values. In the optimal and adjacent conditions, the numerical simulation efficiency and head curves fit well with the test values, while in the partial flow conditions, the numerical simulation head and efficiency are smaller than the test values. Under the optimal working condition, the errors of the head, efficiency, and shaft power between numerical calculation and experimental measurement are 1.5%, 3.2%, and 1.8%, which shows that the numerical calculation method adopted has high accuracy and meets the research requirements.
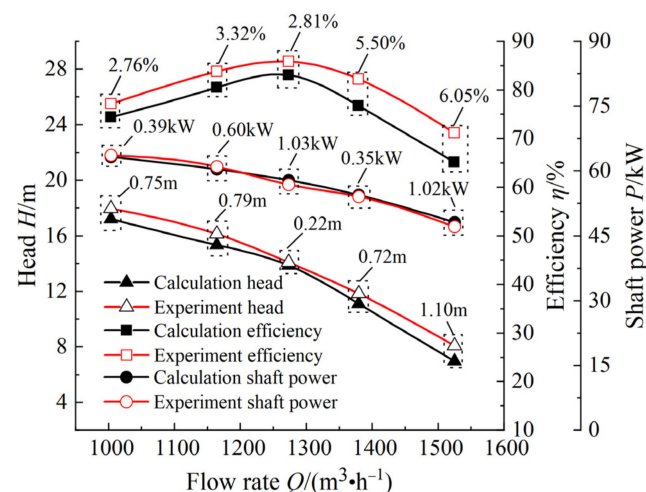

Figure 5. Comparison between numerical simulation and experimental performance characteristics.

2.5. Acoustic Computational Model

The numerical solution of the flow noise field in the pump is essentially unified with the solution of the flow field, and its basic governing equation is the N-S equation. The numerical methods for solving flow-induced noise mainly include a direct method and an indirect method. The direct method is to solve the N-S equation, but this method requires high solving time, model, and boundary conditions. Therefore, in this paper, the indirect method is used to solve the flow-induced noise. The essence of this method is Light hill acoustic analogy method derived from N-S equation, and its governing equation is [15]:

$$\frac{\partial^2 (\rho - \rho_0)}{\partial t^2} - c_0{}^2 \nabla^2 (\rho - \rho_0) = \frac{\partial^2 T_{ij}}{\partial x_i \partial x_j} - \frac{\partial}{\partial x_i} \left\{ \left[(p - p_0)\delta_{ij} \right] \frac{\partial f}{\partial x_j} \delta(f) \right\} + \frac{\partial}{\partial t} \left[\rho_0 u_i \frac{\partial f}{\partial x_j} \delta(f) \right] \qquad (11)$$

where ρ is the fluid density, kg/m^3; ρ_0 represents the average density, kg/m^3; ρ-ρ_0 represents the fluctuation of fluid density, kg/m^3; t is time, s; c_0 is the speed of sound, m/s; x_i is the space coordinate; T_{ij} is the Light hill stress tensor; f is the solid boundary function; ∇ is a splitting operator; p is the flow field pressure, Pa; p_0 is the average value of the flow field pressure, Pa; p-p_0 is the pressure fluctuation in the flow field, Pa; and δ_{ij} is a Kronecker function.

There are three components at the right end of Equation (11), which represent the contribution of quadrupole, dipole, and monopole to the flow-induced noise in the pump.

Backflow and flow separation in the pump are regarded as quadrupole sound sources; The noise caused by dynamic and static interference between the impeller and guide vane belongs to the dipole sound source; the radiation sound source produced by the volume pulsation of fluid medium in the pump is monopole source.

2.6. Acoustic Grid Division and Calculation Setting

The calculation of flow-induced noise of an oblique flow pump is divided into two parts: flow noise and flow radiated noise. Because the impeller is a rotating part in acoustics calculation, it is impossible to simulate its internal sound field in Actran software. Therefore, the calculation domain of flow noise is divided into a pump inlet section and pump guide vane and outlet section fluid domain, as shown in Figure 6a. The calculation domain of flow-radiated noise is the pump casing structure and air radiated sound field, as shown in Figure 6b. The computational domain needs to be meshed in acoustic computation. In the process of computation, the flow information after flow field calculation needs to be interpolated from fluid mesh to acoustic mesh. In this paper, the integral interpolation method is adopted, which interpolates the flow information on the fluid regional grid contained in the acoustic regional grid to the nodes of the acoustic network in the integral form [15].
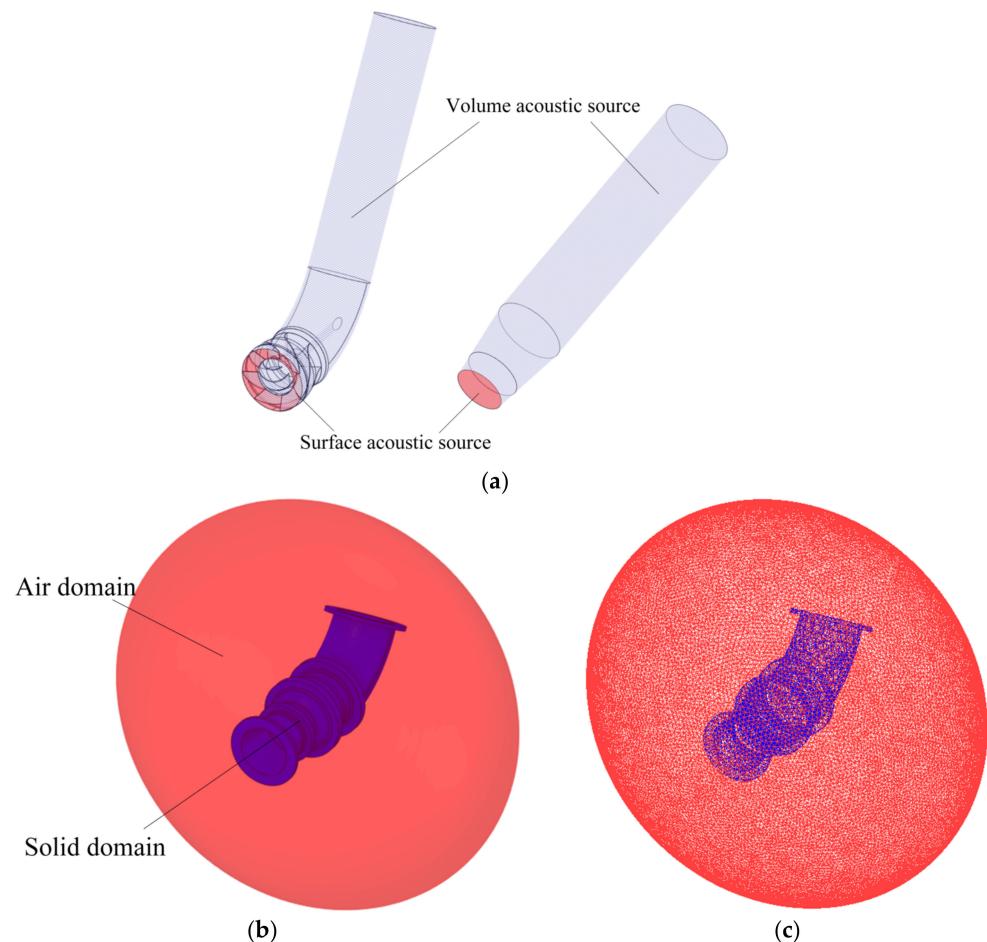

Figure 6. Acoustic calculation settings: (**a**) Flow noise calculation domain and sound source; (**b**) Radiation noise calculation domain; (**c**) Mesh of radiation noise calculation domain.

ANSYS Mesh is still used to divide the acoustic mesh, and the specific form of the flow noise computational domain mesh is roughly the same as that of the flow field computational mesh, so it is no longer shown. The grid division of the computational domain of flow radiated noise is shown in Figure 6c. Although the acoustic grid is sparser than the flow grid, if the grid size is too large, the calculation results will be different. In

general, the maximum size of the acoustic grid should be less than 1/6 of the maximum wavelength of the sound wave, that is [8]

$$L_{max} < \frac{c}{6f_{max}} \tag{12}$$

where L_{max} is the maximum grid size for acoustic calculation, f_{max} is the maximum frequency for acoustic calculation, and c is the speed of sound. According to the calculation step size of unsteady flow, the maximum frequency is 1450 Hz. When the temperature is 20 °C, the sound velocity is 343 m/s in air and 1483 m/s in water. The calculated acoustic grid size should not exceed 39 mm in air and 170 mm in water.

When calculating the flow noise, the acoustic calculation is carried out on the inlet section, the guide vane, and the outlet section. The outlet surface of the inlet section and the inlet surface of the guide vane are, respectively, used as the surface sound source calculated by the two parts, and the fluid area of the two parts is used as the body sound source. The specific arrangement is shown in Figure 6a. Through the ICFD module in Actran software, the time domain information of the variables needed for acoustic calculation is extracted from the flow field calculation results, and then, it is converted to the frequency domain. Finally, the sound field is solved according to the converted frequency domain results.

The calculation process of radiated noise is basically consistent with that of flow noise. The fluid pressure on the fluid–solid interface is extracted and used as the sound source. Different from the flow noise setting, it is necessary to define the air domain and the solid domain and their interface and add boundary conditions and constraints.

3. Results

3.1. Flow Field Analysis

To study the influence of different flow conditions on the pressure field of the whole flow channel of an oblique flow pump, the meridian surface of the flow channel is selected as the research object, and the pressure distribution on the meridian surface is analyzed, as shown in Figure 7. It can be seen from the figure that the pressure in the inlet section is the smallest and the distribution is the most uniform. After the fluid enters the impeller, the pressure increases sharply. With the increase in flow rate, the overall pressure in the flow channel decreases, the pressure distribution gradually tends to be uniform, and the distribution is the most uniform at the optimal working point. The more the flow rate deviates from the optimal operating point, the greater the pressure difference between the impeller inlet and outlet, the more complex the flow in the flow field, and the greater the energy loss.

When the pump is running, the impeller is rotating, but the guide vane is in a static state, so there will be dynamic and static interference between them. To study the degree of the interference and the effect of the interference on the flow field under different flow conditions, the streamline distribution on the unfolding surface of the impeller and guide vane was analyzed. As shown in Figure 8, at the optimal operating point, the streamlines in the impeller and guide vane passages are evenly distributed, and only a small amount of vortex and backflow exists at the outlet of the guide vane blades. Under the condition of a large flow rate, an obvious vortex structure appears at the outlet of the guide vane. However, in the small flow condition, the vortex structure is more obvious. With the decrease in flow rate, the number of vortices gradually increases, and the vortex structure gradually develops from the outlet to the inlet of the guide vane, blocking most of the guide vane flow channels and reducing the flow area at the inlet of the guide vane. The direction of rotation is marked where the vortex is generated in Figure 8. When the flow rate deviates from the optimal operating point, the backflow phenomenon appears in the flow channel, which interacts with the incoming flow in the guide vane and forms a vortex structure, which leads to unstable flow in the guide vane, resulting in a large amount of energy loss and noise problems.
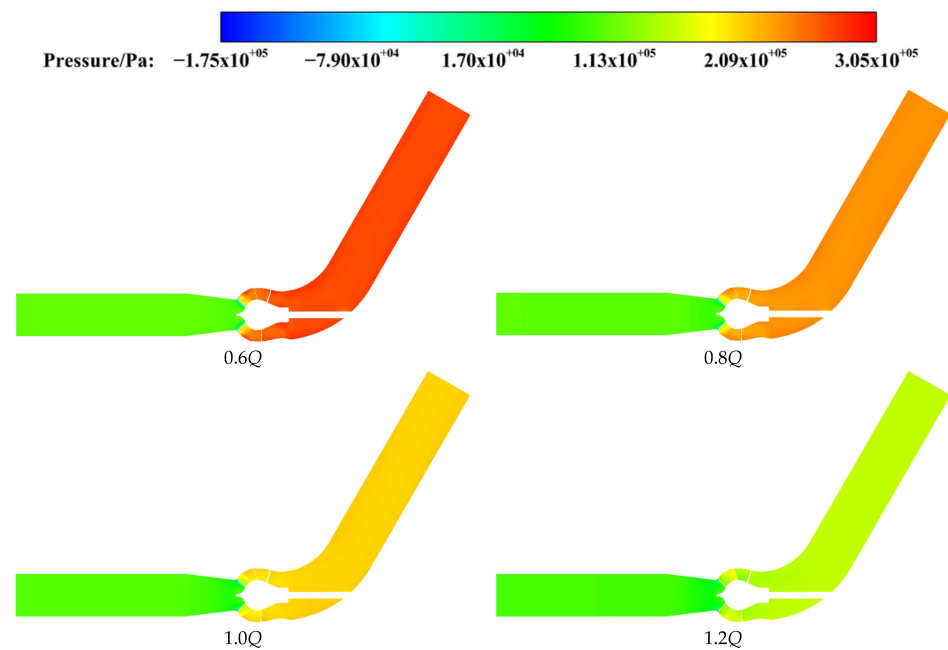
Figure 7. Pressure distributions in the runner under different flow rate conditions.
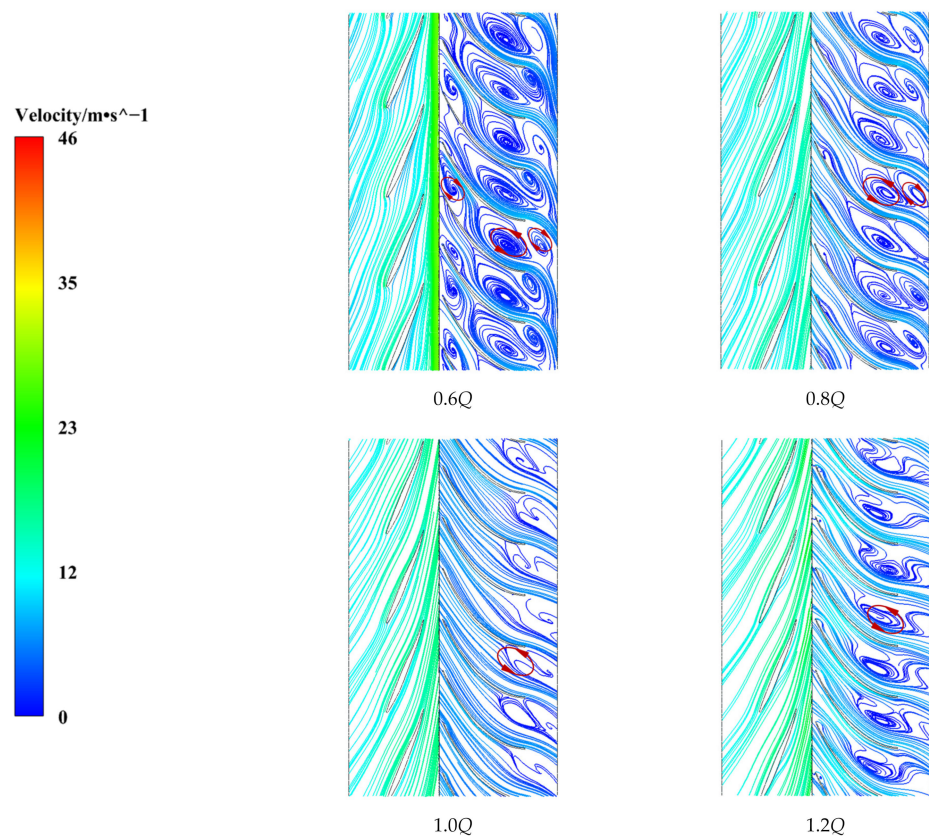
Figure 8. Streamline distributions of the unfolding surface of impeller and guide vane under different flow rate conditions.

The unsteady flow phenomenon in the pump is further studied, and the vortex distribution in the channel is analyzed. Vortex is a common flow state during pump operation. The generation, development, and dissipation of the vortex and the interaction between the vortex and vortex, as well as between the vortex and wall, will arouse the

internal stress of fluid, affect the internal flow field of the oblique flow pump, and cause pressure fluctuation. At the same time, the pressure disturbance will be transmitted in the fluid medium, radiate sound waves outward, and then produce flow-induced noise. In this paper, the *Q*-criterion is used to analyze the flow field. The *Q*-criterion expression is [24]:

$$Q = \frac{1}{2}\left(\|\Omega\|_F^2 - \|S\|_F^2\right) \tag{13}$$

In the formula, $\|\Omega\|_F$ is the norm of the matrix, S is the symmetric part of the velocity gradient tensor, and Ω is the antisymmetric part, which, respectively, represent the deformation and rotation in the corresponding flow field. Therefore, the positive value of the *Q*-criterion represents the physical meaning that vorticity is dominant in the flow field. *Q*-criterion can effectively eliminate the interference of the shear layer on the vortex structure, and the identification of the vortex structure is clearer, more complete, and more accurate.

Figure 9 shows the vorticity distribution in the flow field of the model pump under different flow conditions. It can be seen that high-energy vortices are mostly concentrated in the region of the impeller and guide vane, and the effects of dynamic and static interference and flow separation in this region are significant. The vortex distribution area at the optimal working point is the smallest. Consistent with streamline distribution, there is a large amount of backflow and secondary flow in the impeller and guide vane channel under small flow conditions, which are extremely unstable, with relatively high vortex intensity and a large distribution area. Compared with the small flow condition, the distribution area of the high-energy vortex in the guide vane channel is small under the large flow condition. The vortex distribution trend is different in different guide vane passages, which is caused by the interference between the impeller and the guide vane. In addition, due to the outlet backflow, there are a few high-energy vortices at the inlet of the outlet section.
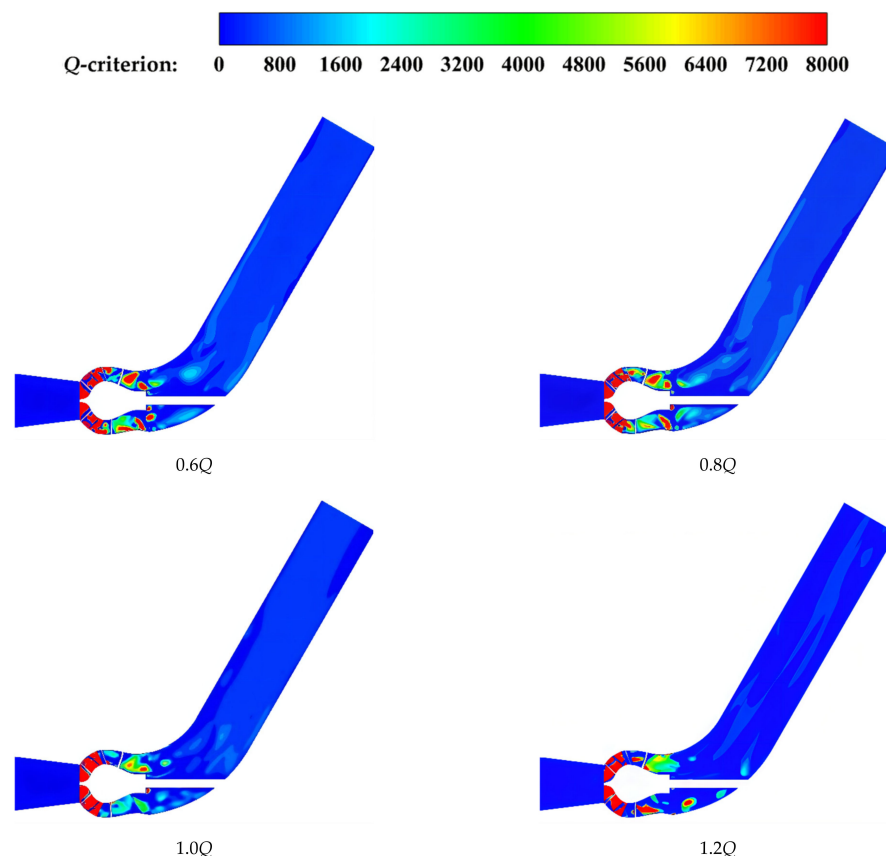

Figure 9. Vorticity distributions under different flow rate conditions.

Furthermore, the vorticity distribution of a guide vane under small flow conditions is studied, and the section of each position of a guide vane under 0.6*Q* is selected as the research object. Figure 10 shows the vorticity distribution at one-third, two-thirds, five-sixths, and the outlet of the guide vane, respectively. The vorticity at the one-third section of the guide vane is mainly distributed in the rim and near the blade, in which the high-energy vortex is near the pressure surface of the blade and extends into the channel, and the medium-energy vorticity is distributed at the hub. With the fluid movement, at the two-third section of the guide vane, the high-energy vortex region concentrates on the pressure surface of the vane and near the rim, and the vorticity region almost spreads all over the channel and uniformly distributes in seven channels, gradually blocking the channels. In the five-sixths section of the guide vane, the vorticity intensity is further enhanced, and the distribution area is further expanded. At the same time, the vorticity attached to the blade ends, and blades shredded with the flow. The vortex shedding at the exit of the guide vane and the trailing edge of the blade merge with the vortex area in the channel to form seven vorticity areas. Although the vortex area in the channel becomes smaller, it still contains a high-energy vortex, which shows that the vortex generated in the channel is not easy to dissipate.
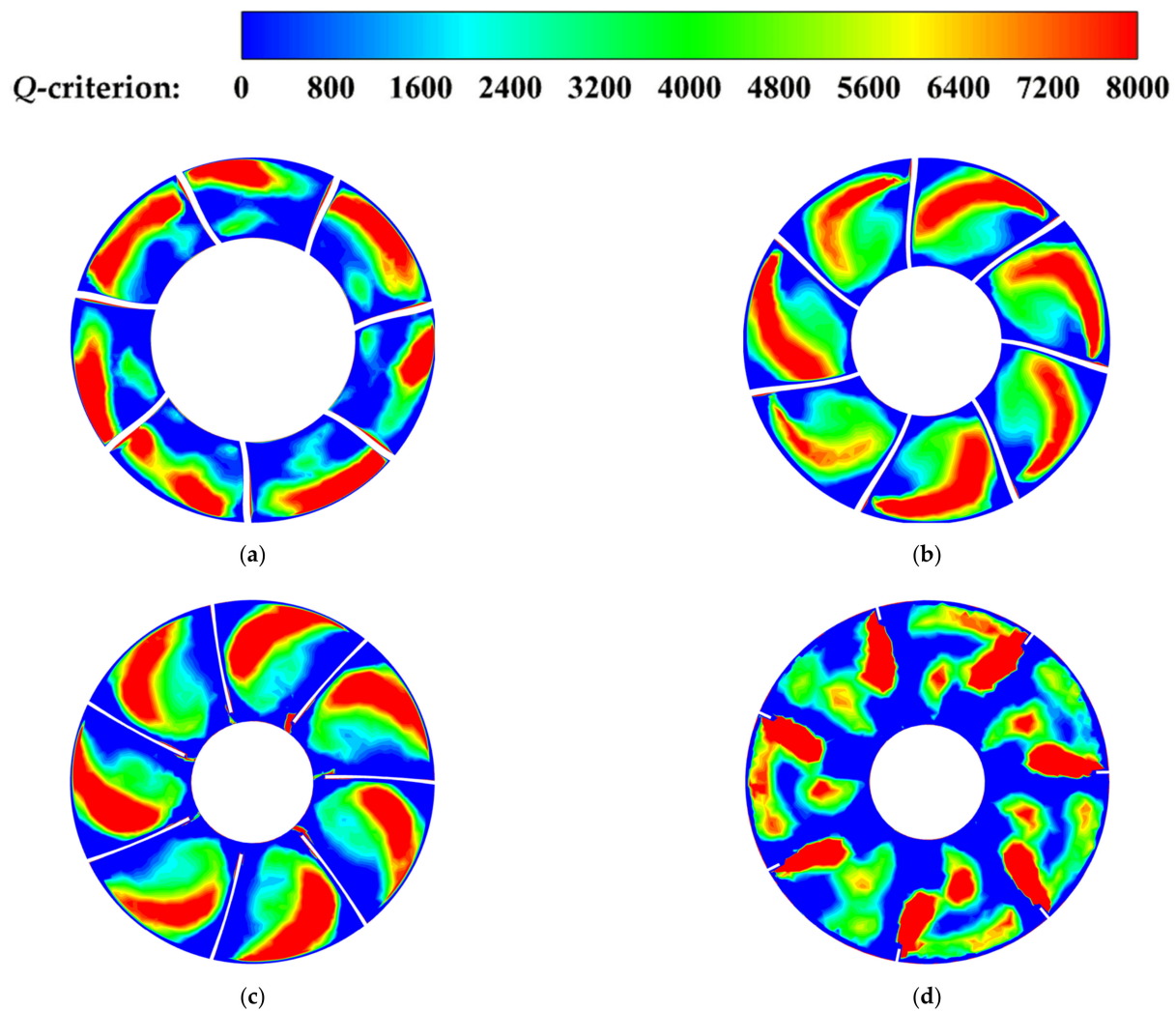

Figure 10. Vorticity distributions on different sections of guide vane. (**a**) One-third of guide vane; (**b**) Two-thirds of guide vane; (**c**) Five-sixths of guide vane; (**d**) Outlet of guide vane.

Through the analysis of vorticity distribution in the guide vane, it can be seen that under the low flow condition, due to the phenomena of backflow and flow separation,

there are more high-energy vortex clusters in the flow channel, and the vortex clusters are distributed in a wide area, which will cause greater flow-induced noise.

3.2. Acoustic Results Analysis

3.2.1. Flow Noise Analysis

The inlet channel sound source includes the surface sound source transmitted by the impeller and the body sound source of the inlet channel itself. The unstable flow in the inlet channel may affect the noise, so it is necessary to analyze the flow noise characteristics in the inlet channel. Figure 11a shows the graph of the flow noise sound pressure level in the inlet channel at the blade frequency (96.6 Hz). It can be seen from the figure that the area with a higher sound pressure level appears at the outlet position of the inlet channel, and the farther away from the outlet position, the lower the sound pressure level. From the radial section, the distribution of sound pressure level presents four regular areas, which are corresponding to the number of blades, indicating that the flow noise in this area is related to impeller interference.
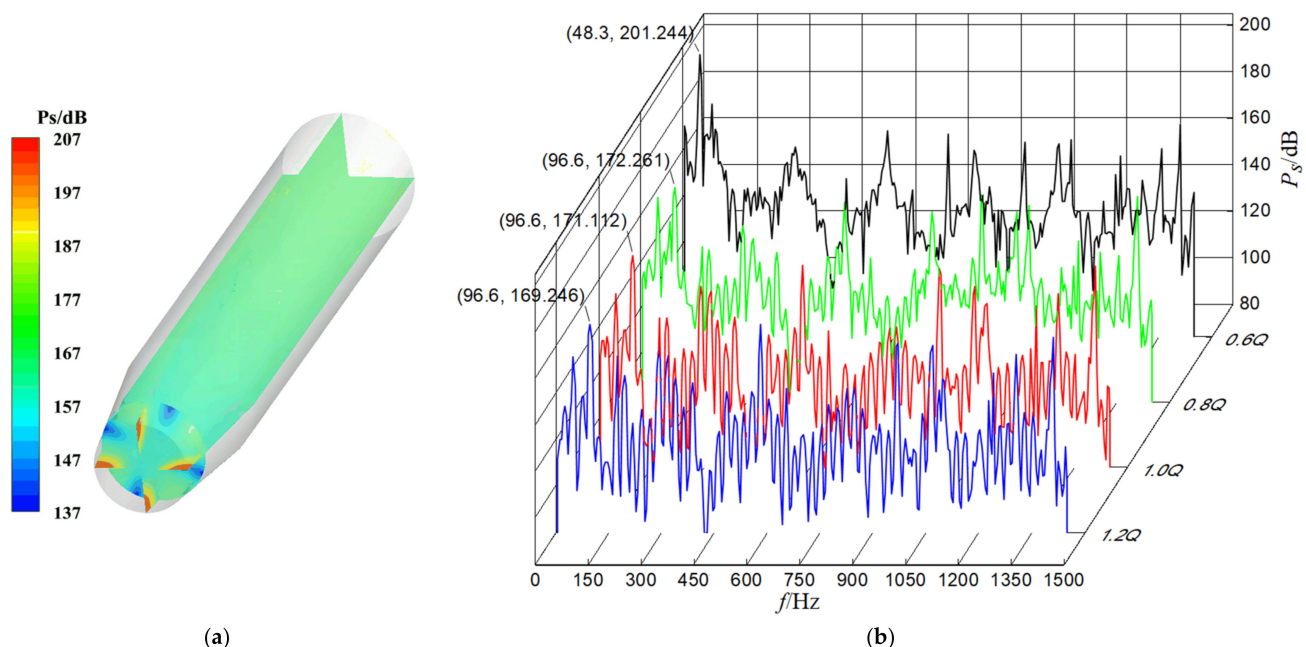

Figure 11. Flow noise results of Inlet area. (**a**) Sound pressure level distribution; (**b**) Spectrum diagram of sound pressure under different flow rate conditions.

Furthermore, the sound pressure spectrum characteristics of inlet channel monitoring points under different flow conditions are compared and analyzed. As shown in Figure 11b, with the increase in flow rate, the sound pressure level of flow noise gradually decreases. The frequency distribution of 0.8Q, 1.0Q, and 1.2Q is basically the same, showing a certain regularity. The maximum peaks all appear at the blade frequency, the rest of the peaks all appear at the frequency doubling position of blade frequency, and the sound pressure intensity is similar everywhere without sudden change. At 0.6Q, the maximum peak appears at half of the blade frequency (48.3 Hz), and the amplitude reaches 201.244 dB.

This result is consistent with the prediction that the noise intensity will increase under the condition of a small flow rate in the previous paper, which also shows that the vortex produced by the unstable flow in the pump channel is one of the sources of noise, and the intensity and distribution area of vorticity will greatly affect the flow noise in the pump.

The sound source of the guide vane and the outlet channel includes the surface sound source transmitted by the impeller and the body sound source of the guide vane and the outlet channel itself. Because of the dynamic and static interaction between the impeller and the guide vane as well as the backflow and other factors, the flow inside the guide vane

and the outlet channel is more complex, leading to more unstable flow, so it is necessary to study the flow noise characteristics in the guide vane and the outlet channel. Figure 12 shows the sound pressure level distribution of the guide vane and outlet channel under different flow conditions, and the blade frequency (96.6 Hz) is selected for analysis.
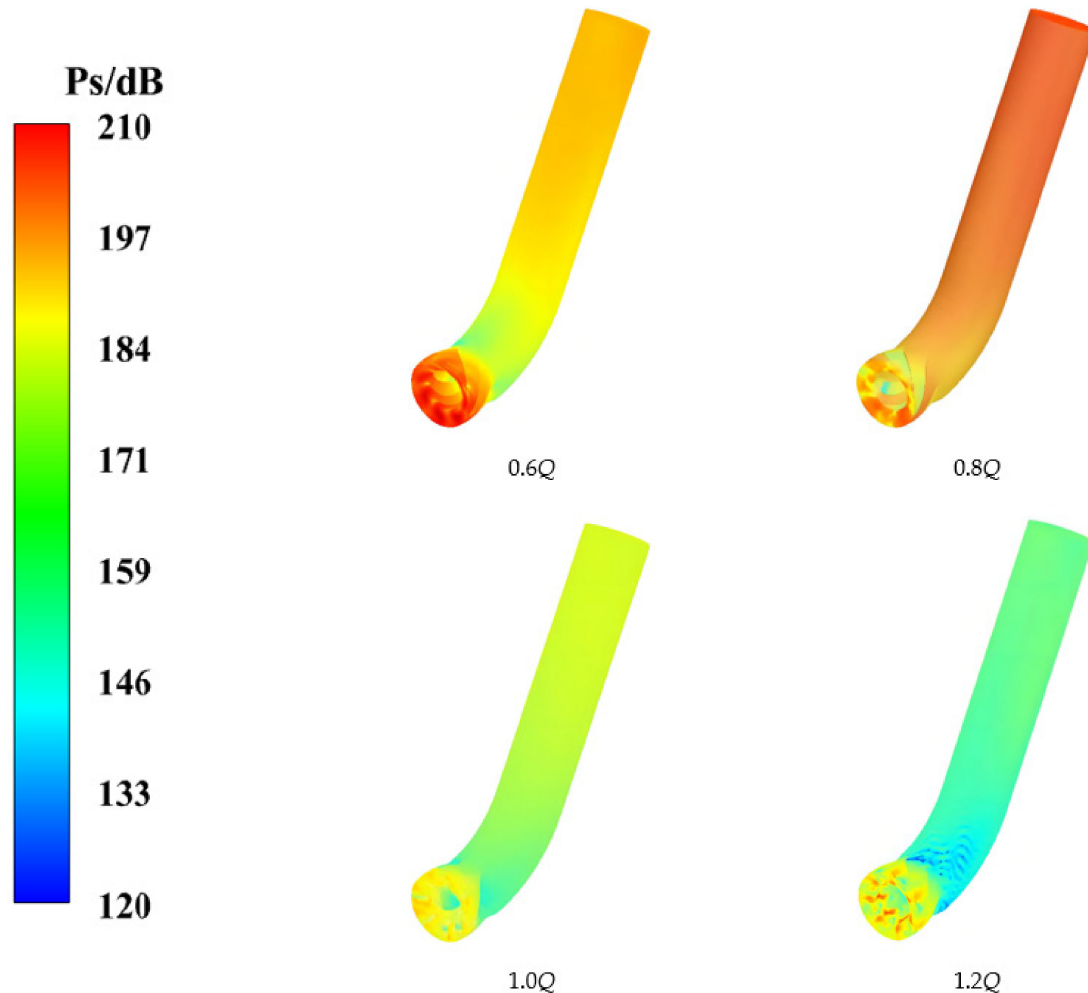

Figure 12. Sound pressure level distribution of guide vane and outlet area under different flow rate conditions.

It can be seen from the figure that from the guide vane to the outlet of the flow channel, the noise sound pressure level first decreases and then increases, and the sound pressure level inside the guide vane is the highest. For the guide vane area, with the increase in flow rate, the sound pressure level first decreases and then increases, and the sound pressure level is the lowest at 1.0*Q*: that is, the noise generated by the flow is the smallest, which corresponds to the conclusion of the previous flow field analysis. Under optimal working conditions, the flow in the guide vane is the most stable, and the vortex and backflow are the least stable. For the pump outlet channel area, generally speaking, with the increase in flow rate, the noise sound pressure level gradually decreases. The noise pressure level distribution in the whole area is uniform.

Furthermore, the frequency domain characteristics of sound pressure at different positions in the guide vane are studied. As shown in Figure 13a, three monitoring points are set in the axial direction inside the guide vane, and the sound pressure frequency domain characteristics of the three monitoring points are compared and analyzed. Because of the similarity of frequency domain distribution of monitoring points under different flow conditions, the spectrum diagram under the optimal working condition is selected

for analysis, as shown in Figure 14. The spectrum diagram in Figure 14 is filtered. The frequency distribution law of the three monitoring points is basically the same, and the maximum peak appears at the axial frequency (24.15 Hz). Then, the sound pressure fluctuation gradually stabilizes. The sound pressure intensity decreases gradually from the inlet to the outlet of the guide vane in the low-frequency and medium low-frequency regions. This shows that in the guide vane, the influence of static and dynamic interference between the impeller and the guide vane gradually weakens with the distance from the impeller.
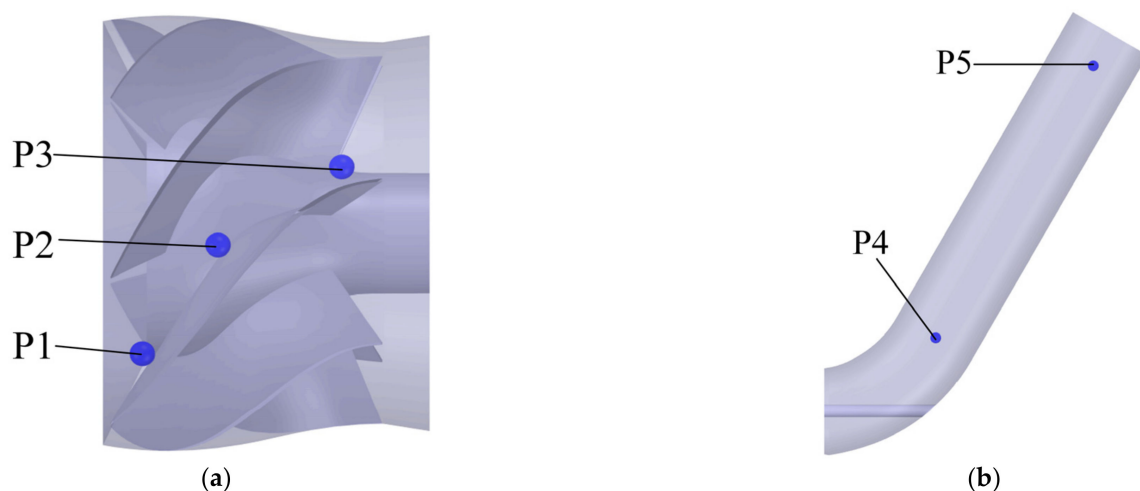

(**a**)   (**b**)

Figure 13. Schematic diagram of monitoring points. (**a**) Monitoring points in guide vane; (**b**) Monitoring points in outlet.
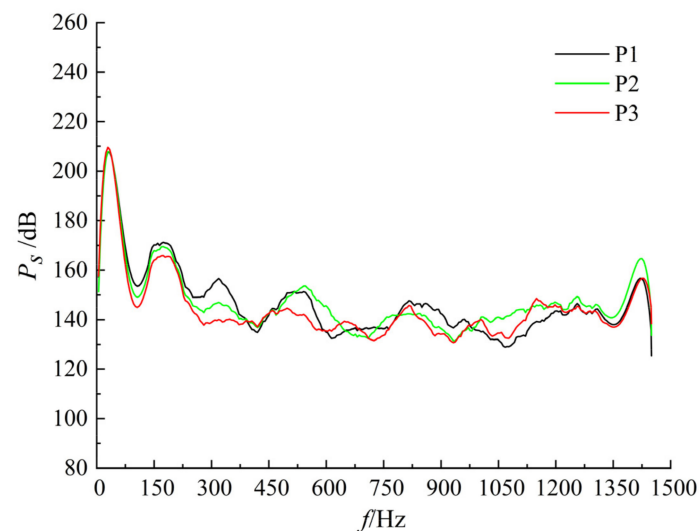

Figure 14. Spectrum diagram at monitoring points of guide vane.

The frequency domain characteristics of sound pressure at different positions in the exit area are studied. As shown in Figure 13b, two monitoring points are set in the outlet pipe along the flow direction. The frequency domain distribution of monitoring points under optimal working conditions is studied. The frequency domain distribution characteristics of the two monitoring points are compared and analyzed. It can be seen from Figure 15 that the maximum peaks of two points appear at the axial frequency. The spectrum diagram in Figure 15 is filtered. In the first half of the spectrum, the sound pressure intensity at the P5 point is higher than that at the P4 point. In the second half of the spectrum, the result is just the opposite.
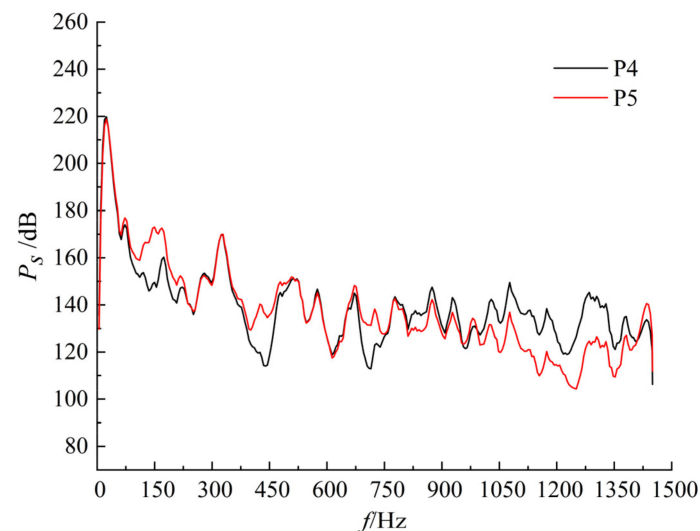
Figure 15. Spectrum diagram at monitoring points of the outlet area.

3.2.2. Flow-Induced Radiated Noise Analysis

Unstable flow in the pump will aggravate the pressure pulsation in the pump, and the pressure generated by the fluid will cause structural vibration on the pump body, resulting in radiation noise, which will have an impact on the staff and the environment. Therefore, it is necessary to study the flow-induced radiated noise of oblique flow pumps.

To check the directional distribution and radiation level of flow-induced radiated noise of the oblique flow pump, it is necessary to set up monitoring points around the pump. On the radial plane, a circle of monitoring points is uniformly set with a radius of 1 m from the outer wall of the pump. To close the acoustic pointing curve, a total of 61 monitoring points are set, as shown in Figure 16. In Figure 16, the sound pressure radiation level of the external sound field under different flow conditions at the blade frequency is analyzed. It can be seen from the figure that due to the unified scale, the sound pressure distribution in the radial plane of small flow conditions presents an approximate circle shape, and in fact, all flow conditions can show obvious dipole characteristics. With the increase in flow rate, the radiation level of sound pressure increases, showing low radiation levels under large flow rates and high radiation levels under small flow rates. It can be seen that the unsteady flow under the condition of a small flow rate will also have a great influence on the radiated noise of the pump.
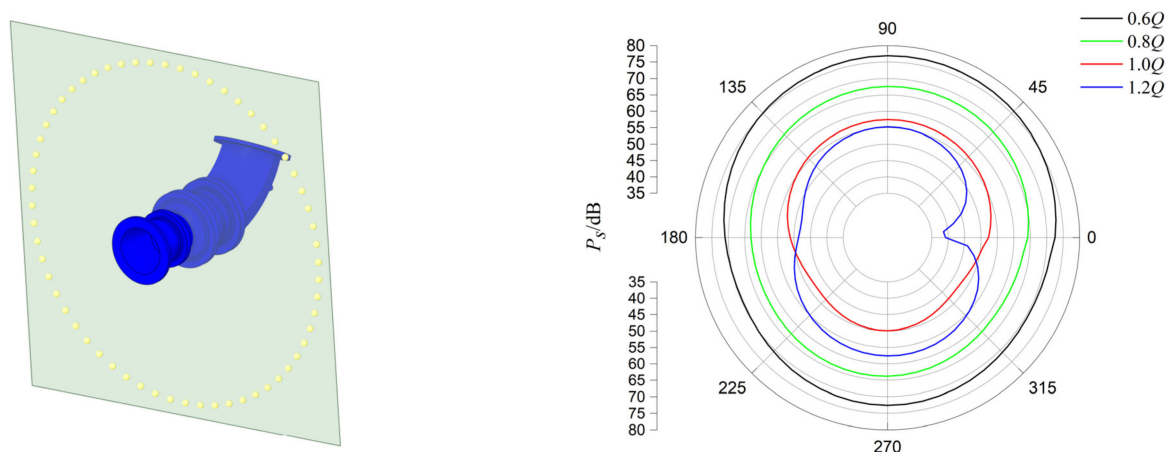

Figure 16. Schematic diagram of monitoring points and radiation noise directivity under different flow rate conditions.

4. Conclusions

In this paper, the flow field and sound field of the oblique flow pump are numerically calculated. The internal flow characteristics and flow-induced noise characteristics of the oblique flow pump were studied. The main conclusions are as follows:

(1) At the optimal operating point, the streamlines in the impeller and guide vane of the oblique flow pump are evenly distributed, and only a small amount of vortex and backflow exists at the outlet of the guide vane. When the flow rate deviates from the optimal operating point, the flow channel appears to have a backflow phenomenon, which interacts with the incoming flow in the guide vane, and the flow is extremely unstable, forming a vortex structure with relatively high vortex intensity and a large distribution area. Under the condition of a small flow rate, due to the phenomenon of backflow and flow separation, there are many high-energy vortices in the flow channel, and the vortices are distributed in a wide area, which will cause large flow-induced noise. In addition, due to the outlet backflow, there are a few high-energy vortices at the inlet of the outlet section.

(2) A higher sound pressure level of flow noise in the inlet channel appears at the outlet position of the inlet channel, and the farther away from the outlet position, the lower the sound pressure level. With the increase in flow rate, the sound pressure level of flow noise gradually decreases. The frequency domain distributions at $0.8Q$, $1.0Q$, and $1.2Q$ are the same, showing a certain regularity, and the maximum peaks appear at the blade frequency (96.6 Hz). At $0.6Q$, the maximum peak appears at half of the blade frequency (48.3 Hz), and the amplitude reaches 201.244 dB. This result shows that the vortex generated by the unstable flow in the pump channel is one of the sources of noise, and the intensity and distribution area of vorticity will greatly affect the flow noise in the pump.

(3) From the guide vane to the outlet of the flow passage, the sound pressure level of flow noise first decreases and then increases, and the sound pressure level in the guide vane is the highest. For the guide vane area, with the increase in flow rate, the sound pressure level first decreases and then increases, and the sound pressure level is the lowest at $1.0Q$. In the low-frequency and middle-low-frequency areas, the sound pressure intensity gradually decreases from the inlet to the outlet of the guide vane. In the pump outlet channel area, generally speaking, with the increase in flow rate, the noise sound pressure level gradually decreases. In the first half of the spectrum, along the flow direction, the sound pressure intensity increases. In the second half of the spectrum, the result is just the opposite.

(4) At the blade frequency, the radiated noise of the oblique flow pump can show dipole characteristics under various flow conditions. With the increase in flow rate, the radiation level of sound pressure increases, showing low radiation levels under large flow rates and high radiation levels under small flow rates. Unstable flow under small flow conditions will also have a great impact on the radiated noise of the pump.

This paper can provide a theoretical basis for the mechanism research and control strategy of flow-induced noise of oblique flow pump and provide some reference for developing oblique flow pump with low noise and high stability. Some studies in this paper can be further studied, such as comparing the difference of flow noise at radial monitoring points.

Author Contributions: Conceptualization, F.Z. (Fan Zhang); Data curation, F.Z. (Feifei Zhao) and J.L.; Resources, M.S.; Supervision, F.Z. (Fan Zhang) and J.Z.; Writing—Original draft, Z.X. All authors have read and agreed to the published version of the manuscript.

Conflicts of Interest: The authors declare no conflict of interest.

References

1. Li, W.; Ji, L.; Shi, W.; Zhou, L.; Jiang, X.; Zhang, Y. Fluid-structure interaction study of a mixed-flow pump impeller during startup. *Eng. Comput.* **2018**, *35*, 18–34. [CrossRef]
2. Li, W.; Zhang, Y.; Shi, W.; Ji, L.; Yang, Y.; Ping, Y. Numerical simulation of transient flow field in a mixed-flow pump during starting period. *Int. J. Numer. Methods Heat Fluid Flow* **2018**, *28*, 927–942. [CrossRef]
3. Miyabe, M.; Maeda, H.; Umeki, I.; Jittani, Y. Unstable head-flow characteristic generation mechanism of a low specific speed mixed flow pump. *J. Therm. Sci.* **2006**, *15*, 115–120. [CrossRef]
4. Li, Y.; Li, R.; Wang, X. Large Eddy Simulation of Unsteady Flow in a Mixed Flow Pump Guide Vane. *Appl. Mech. Mater.* **2014**, *444–445*, 555–560. [CrossRef]
5. Dong, L.; Dai, C.; Kong, F.; Fu, L.; Cao, R. Flow-induced Noise Characteristic and Contribution to Interior Noise for Centrifugal Pump as Turbine. *J. Mech. Eng.* **2016**, *52*, 184–192. [CrossRef]
6. Guo, R.; Li, R.; Zhang, R. Characteristic Analysis of Interior Hydrodynamic Noise in Jetting Centrifugal Pump. *Trans. Chin. Soc. Agric. Mach.* **2018**, *49*, 156–164.
7. He, A.; Shao, C. Study on the induced noise of gas–liquid two-phase flow in a centrifugal pump. *Appl. Acoust.* **2021**, *176*, 107892. [CrossRef]
8. Si, Q.; Shen, C.; He, X.; Li, H.; Huang, K.; Yuan, J. Numerical and Experimental Study on the Flow-Induced Noise Characteristics of High-Speed Centrifugal Pumps. *Appl. Sci.* **2020**, *10*, 3105. [CrossRef]
9. Wang, Y.; Ding, Z. Influence of blade number on flow-induced noise of centrifugal pump based on CFD/CA. *Vacuum* **2020**, *172*, 109058.
10. Choi, J.-S.; McLaughlin, D.K.; Thompson, D.E. Experiments on the unsteady flow field and noise generation in a centrifugal pump impeller. *J. Sound Vib.* **2003**, *263*, 493–514. [CrossRef]
11. Dai, C.; Guo, C.; Chen, Y.; Dong, L.; Liu, H. Analysis of the Influence of Different Bionic Structures on the Noise Reduction Performance of the Centrifugal Pump. *Sensors* **2021**, *21*, 886. [CrossRef] [PubMed]
12. Wang, H.; Xu, X.; Yang, A.; Wang, F.; Tan, Y. Numerical simulation of flow noise in axial-flow pump. *J. Drain. Irrig. Mach. Eng.* **2011**, *29*, 199–203. (In Chinese)
13. Pan, Y.; Li, Y.; Huang, M.; Liao, Y.; Liang, D. Noise source identification and transmission path optimisation for noise reduction of an axial piston pump. *Appl. Acoust.* **2018**, *130*, 283–292. [CrossRef]
14. Li, Q.; Liang, N.; Tong, W.; Xu, H.; Cao, L.; Wu, D. Research on flow-induced noise properties of waterjet pump based on cyclostationary method. *J. Zhejiang Univ. Eng. Sci.* **2021**, *55*, 1660–1667.
15. Zhang, F.; Zhu, L.-F.; Shi, X.-T.; Chen, K.; Appiah, D.; Yuan, S.-Q.; Zhang, J.-F. Influence of pump noise on the health of fish in a large pumping station. *J. Hydrodyn.* **2022**, *34*, 522–531. [CrossRef]
16. Yang, Y.; Li, W.; Shi, W.; Ping, Y.; Yang, Y.; Wang, L. Numerical investigation on the unstable flow at off-design condition in a mixed-flow pump. *Proc. Inst. Mech. Eng. Part A J. Power Energy* **2019**, *233*, 849–865. [CrossRef]
17. Han, Y.; Tan, L. Influence of rotating speed on tip leakage vortex in a mixed flow pump as turbine at pump mode. *Renew. Energy* **2020**, *162*, 144–150. [CrossRef]
18. Sedlar, M.; Komárek, M.; Vyroubal, M.; Doubrava, V.; Varchola, M.; Hlbočan, P. Experimental and numerical analysis of unsteady behaviour of high efficiency mixed-flow pump. *EPJ Web Conf.* **2014**, *67*, 2104. [CrossRef]
19. Zhang, W.; Zhu, B.; Yu, Z.; Yang, C. Numerical study of pressure fluctuation in the whole flow passage of a low specific speed mixed-flow pump. *Adv. Mech. Eng.* **2017**, *9*, 168781401770765. [CrossRef]
20. Hao, B.; Cao, S. Experimental study of the influence of flow passage subtle variation on mixed-flow pump performance. *Chin. J. Mech. Eng.* **2014**, *27*, 615–621.
21. Li, W.; Zhou, L.; Ji, L.; Shi, W.; Jiang, X.; Zhang, Y. Vibration characteristics of the impeller at multi-conditions in mixed-flow pump under the action of fluid-structure interaction. *J. Vibroeng.* **2016**, *18*, 3213–3224. [CrossRef]
22. Xu, Z.; Zhang, F.; Chen, K.; Zhu, L.F.; Zhang, J.F.; Song, M.F. Study on the Rotor Dynamic Characteristics of an Oblique Flow Pump under the Action of Fluid-structure Interaction. *Trans. Chin. Soc. Agric. Mach.* **2022**, 1–12. Available online: http://kns.cnki.net/kcms/detail/11.1964.s.20220915.1444.032.html (accessed on 16 September 2022).
23. Menter, F.; Kuntz, M.; Langtry, R. Ten Years of Industrial Experience with the SST Turbulence Model. *Heat Mass Transf.* **2003**, *4*, 625–632.
24. Hunt, J.; Wray, A.; Moin, P. Eddies, Streams, and Convergence Zones in Turbulent Flows. J. Studying Turbulence Using Numerical Simulation Databases, 2. Proceedings of the 1988 Summer Program. 1988. Available online: https://ntrs.nasa.gov/citations/19890015184 (accessed on 16 September 2022).